Stellar *s*-process neutron capture cross sections of ^{69,71}Ga

M. Tessler,[1,2,*] M. Paul,[2] S. Halfon,[1] Y. Kashiv,[3] D. Kijel,[1] A. Kreisel,[1] A. Shor,[1] and L. Weissman[1]

[1]*Soreq Nuclear Research Center, Yavne 81800, Israel*

[2]*Racah Institute of Physics, Hebrew University, Jerusalem 91904, Israel*

[3]*University of Notre Dame, Notre Dame, Indiana 46556, USA*

(Received 10 September 2021; revised 29 November 2021; accepted 2 February 2022; published 8 March 2022)

The stable gallium isotopes, ^{69,71}Ga, are mostly produced by the weak slow (*s*) process in massive stars. We report here on measurements of astrophysically relevant neutron capture cross sections of the ^{69,71}Ga(n,γ) reactions. The experiments were performed by the activation technique using a high-intensity ($3–5\times10^{10}$ n/s), quasi-Maxwellian neutron beam that closely mimics conditions of stellar *s*-process nucleosynthesis at $kT\approx40$ keV. The neutron field was produced by a mA proton beam at $E_p=1925$ keV (beam power of 2–3 kW) from the Soreq Applied Research Accelerator Facility (SARAF), bombarding the liquid-lithium target (LiLiT). A 473-mg sample of Ga_2O_3 of natural isotopic composition was activated in the LiLiT neutron field and the activities of ^{70,72}Ga were measured by decay counting via γ spectrometry with a high-purity germanium detector. The Maxwellian-averaged cross sections at $kT=30$ keV of ^{69}Ga and ^{71}Ga determined in this work are 136(8) and 105(7) mb, respectively, in good agreement with previous experimental values. Astrophysical implications of the measurements are discussed.

DOI: 10.1103/PhysRevC.105.035801

I. INTRODUCTION

The majority of elements beyond iron are produced by neutron capture reactions in stars. The slow neutron capture process (*s* process) is composed of the weak and main components [1]. The main component takes place during recurrent thermal pulses in the He shell of low-mass AGB stars ($M\lesssim4M_\odot$). The weak component is produced during core He and shell C burning in massive stars ($M\gtrsim8M_\odot$). Neutron densities during the *s* process are between 10^6 and 10^{12} n/cm^3 [2]. The weak *s* process produces most of the *s*-process isotopes between iron and strontium ($60<A<90$). Figure 1 shows the weak *s*-process flow in the Ga region. Recent simulations show that gallium is the most abundant *s* element at the end of shell carbon burning in a model of $25M_\odot$ star [3].

Until recently, there was only a time-of-flight (TOF) measurement of the ^{69}Ga(n,γ) cross section, with a sample of natural gallium [4] (see also [5]). Other nuclei measured within the same experimental campaign (^{74}Ge, ^{75}As, ^{81}Br) show large deviations from more recent results [5]. For ^{71}Ga, two previous results from activation measurements are in marginal agreement [6,7]. Very recently, values were published for the neutron capture cross sections of ^{69,71}Ga [8] which are stated to disagree with available evaluated data from KADoNiS v0.3 [5]. We report here on new measurements of the ^{69,71}Ga(n,γ) cross sections, which were initiated prior to the publication of the latter results. This work took advantage of the liquid-lithium target (LiLiT) at the Soreq Applied Research Accelerator Facility (SARAF) intense quasi-Maxwellian neutron source ([9], see Sec. II), especially valuable for the activation measurement of short-lived nuclides like ^{70}Ga ($t_{1/2}=21.1$ min). Section II describes the SARAF-LiLiT neutron source, Sec. III describes the samples used and the irradiation details, and Sec. IV describes the activity measurements. In Sec. V we report the activation results, in Sec. VI we calculate the experimental cross sections, Sec. VII describes how the MACSs were calculated, and in Sec. VIII we discuss the results.

II. SARAF-LILIT

An intense ^{7}Li$(p,n)^7$Be neutron source, in the form of a liquid-lithium target (LiLiT) [10,11], bombarded by a mA proton beam from the Soreq Applied Research Accelerator Facility (SARAF), was developed and is used for Maxwellian average cross section (MACS) measurements. The SARAF accelerator is based on a continuous wave (cw), proton/deuteron RF superconducting linear accelerator. SARAF phase I, presently undergoing a major upgrade to its phase II, consisted of a 20 keV/u electron cyclotron resonance (ECR) ion source injector, a low-energy beam transport section (LEBT), a four-rod radio frequency quadrupole (RFQ, 1.5 MeV/u), a medium energy beam transport section (MEBT), a prototype superconducting module (PSM) housing six half-wave resonators and three superconducting solenoids, and a diagnostic plate (D plate). The beamline downstream of the accelerator transports the high intensity beam to the target. SARAF phase I delivered for experiments currents of up to 2 mA of protons or deuterons, with energies of up to ≈4 and 5 MeV, respectively [12–14].

*Corresponding author: moshe.tessler@mail.huji.ac.il

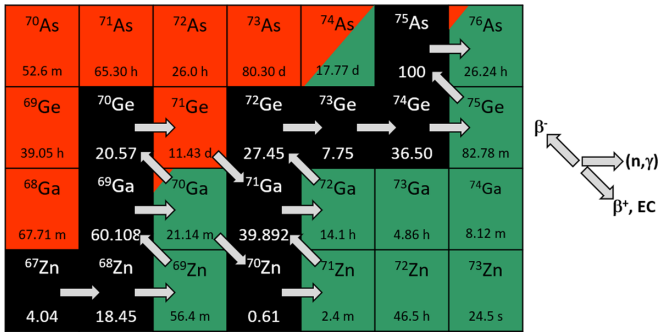

FIG. 1. The path of the *s* process between zinc and arsenic. The numerical values are the terrestrial isotopic abundances in % (half-life) for stable (unstable) nuclides. When ^{69}Ga captures a neutron, the product ^{70}Ga either decays to ^{70}Ge (99.59%) or to ^{70}Zn (0.41%) with a half-life of 21.14 min. Following the neutron capture reaction on ^{71}Ga, the product ^{72}Ga decays to ^{72}Ge with a half-life of 14.1 h.

The SARAF high-intensity beam requires a Li target that can withstand its power, which is incompatible with solid Li and Li compounds. The liquid-lithium target (LiLiT) [10,11] consists of a liquid-lithium film (temperature ≈200 °C, above the lithium melting temperature of 180.5 °C) circulated at high velocity (3–7 m/s) onto a thin convex stainless-steel support wall. The target is bombarded with a high-intensity proton beam impinging directly on the Li-vacuum (windowless) interface at an energy above and close to the ^{7}Li(p, n) reaction threshold, $E_{th} = 1.88$ MeV (Fig. 2). A rectangular-shaped nozzle just upstream of the curved support wall determines the film width and thickness to be 18 and 1.5 mm, respectively (see [10] for details). The first few microns at the surface of the liquid-lithium film serve as the neutron-producing thick target. The deeper Li film layers act as a beam dump, from which the power is transported by the flow to a heat exchanger. A spherical cap made of stainless steel foil, 0.5 mm thick and 19 cm in diameter, is located ≈1 mm beyond the nozzle and seals the LiLiT vacuum chamber neutron exit port (Fig. 2). The vacuum wall curvature (convex toward the Li flow with a curvature radius of 300 mm) allows us to locate a secondary activation target very close (see below) to the neutron source at the Li-vacuum interface.

III. SAMPLE CHARACTERISTICS AND IRRADIATION DETAILS

In the experiment described here, a 13-mm-diameter $^{nat}Ga_2O_3$ (99.99+% purity [15]) pellet target was activated. It was sandwiched between two Au foils (Table I) which were used as monitors of the neutron fluence. The distance of the 13-mm-diameter Ga target from the Li neutron source was 6 ± 1 mm, intercepting >75% of the outgoing neutrons. The characteristics of the samples used are summarized in Table I.

The Ga and Au targets were inserted into the LiLiT activation chamber (Fig. 2) and held in place by the target holder. The 9-mm full width proton beam impinged on the free-surface lithium film, resulting in an outgoing neutron cone due to the ^{7}Li(p, n) reaction, which irradiated the target. The setup is shown in Fig. 2 and explained in the caption.

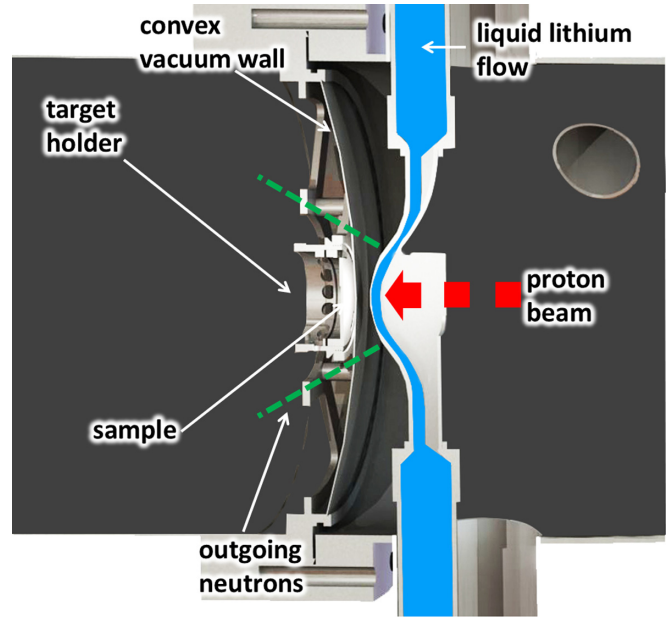

FIG. 2. Diagram of the liquid-lithium target (LiLiT) and activation target assembly. The 1–2 mA (≈9 mm full width) proton beam (dashed red arrow) impinges directly on the windowless liquid-lithium film. The light blue shows the liquid-lithium circulating flow (see [10] for details). The activation samples are mounted at the center of a ring target holder made of Al and positioned in the outgoing neutron cone (green dashed lines) at a distance of ≈6 mm from the liquid-lithium film surface. The targets are in a vacuum chamber separated from the LiLiT chamber by a 0.5 mm stainless steel concave vacuum wall.

The number of stable nuclei A per cm^2, $n_t(A)$, for a target element with an atomic or molecular mass M_A, target area S, and mass m, is given by Eq. (1):

$$n_t(A) = s_A a(A) \frac{mN_A}{SM_A}. \quad (1)$$

The symbol N_A denotes Avogadro's number and $a(A)$ the isotopic abundance of A (Table II). The stoichiometry of element

TABLE I. Characteristics of the samples used in this work. They are listed in the order that they were placed downstream from the Li target. The first gold foil (Au no. 33) was necessary to monitor the beam offset (see below). The Ga oxide targets no. 2 (no. 1) were used for neutron irradiations above (below) the Li neutron emission threshold.

Sample	Diam. (mm)	Mass (mg)	Nucleus	n_t (10^{19} cm^{-2})
Au no. 33	25	109.8(1)	^{197}Au	6.839(4)
Au no. 14	13	31.6(1)	^{197}Au	7.28(1)
$^{nat}Ga_2O_3$ no. 2	13	472.5(1)	^{69}Ga	137.5(1)
			^{71}Ga	91.25(1)
Au no. 15	13	32.5(1)	^{197}Au	7.49(1)
$^{nat}Ga_2O_3$ no. 1	13	443.0(1)	^{69}Ga	128.9(1)
			^{71}Ga	85.55(1)

TABLE II. Properties of the relevant target and product nuclei studied in this work. The half-life data were taken from [17,20,21].

Target nucleus	Isotopic abundance	Product nucleus	Half-life, $t_{1/2}$
^{197}Au	1	^{198}Au	2.6947(3) d
^{69}Ga	0.601 08(9)	^{70}Ga	21.14(5) m
^{71}Ga	0.398 92(9)	^{72}Ga	14.10(1) h

A in the target is denoted by s_A ($s_A = 2$ or 1 for Ga or Au, respectively).

The proton beam energy was measured by a TOF pick-up and Rutherford backscattering off a Au target located in the diagnostic D plate. The beam energy was 1925 keV, with an energy spread of ≈15 keV. The energy spread was estimated from beam dynamics calculations and was verified experimentally under similar conditions [16].

To determine the position of the proton beam relative to the activation targets, the 25-mm-diameter gold foil (Au no. 33) was autoradiographically scanned after the samples irradiation (Fig. 3). An offset of 2.5 mm in the vertical direction was found and accounted for in our detailed simulations.

Throughout the irradiation, the neutron yield was continuously monitored and recorded with a fission-product ionization chamber detector (PFC16A, Centronics Ltd.), counting neutron-induced fission events from a thin ^{235}U internal foil (1 mg/cm^2, 12.5 cm^2 active area). The fission chamber was located at 0° to the incident proton beam, at a distance of ≈80 cm downstream from the target. The fission chamber was covered with a 1-mm-thick Cd sheet to absorb scattered thermal neutrons. The count rate of the fission

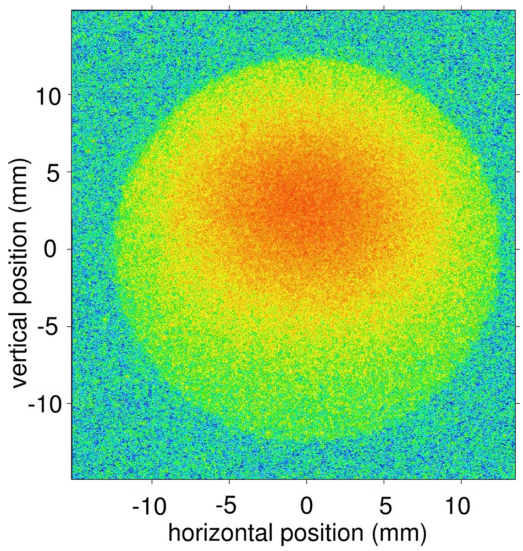

FIG. 3. An autoradiographic scan of the 25-mm-diameter gold foil (Au no. 33). Red indicates the area with the highest neutron irradiation followed by yellow, green and blue. A ≈2.5-mm offset was observed in the neutron irradiation and is attributed to the vertical steering of the proton beam. This offset was taken into account in the neutron irradiation simulations.

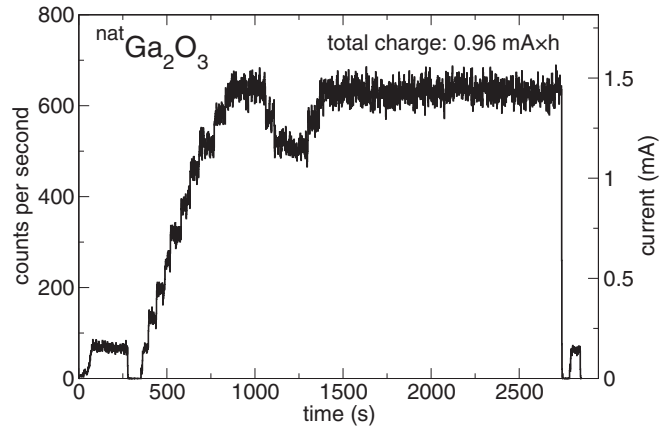

FIG. 4. Time record of the fission chamber count rate (left axis) and corresponding intensity of the proton beam current (right axis) during the irradiation. The two low-intensity intervals and gaps at beginning and end of the irradiation correspond to the calibration of the fission count rate against beam current measured at low intensity with a Faraday cup (see text). All intensity variations are taken into account by the $1/f_b$ correction factor [Eq. (2)]. The total integrated current was 0.96 mA × h.

chamber was calibrated to the beam current at low intensity (10% duty cycle, using a slow chopper), with the Faraday cup located ≈1 m upstream of the Li target. After the SARAF was tuned, the beam duty cycle was ramped up to 99%. Normally, the ramp up is performed rather slowly while monitoring the temperature and radiation along the beamline and LiLiT. If necessary, fine-tuning of the beamline ion-optical magnetic elements (bending magnets, steerers) is performed based on temperature reading of sensors located on the lithium nozzle (see [10,11] for details). It is important to know the time dependence of the neutron yield in the case of a short-lived activation product (e.g., ^{70}Ga, $t_{1/2} = 21.1$ min). In such a case, one needs to account for fluctuations of the neutron yield when evaluating the fraction of the reaction product that decayed during the irradiation. The time record of the proton beam current is presented in Fig. 4. The total integrated current in the irradiation was ∼0.96 mA × h.

IV. ACTIVITY MEASUREMENT

After the irradiation, the induced activities were measured separately for each sample with a shielded HPGe detector (ORTEC GMX 25-83). The distance of the sample to the HPGe detector was 20 cm (2 cm) for the measurement above (below) the neutron threshold. The detector efficiency was determined by standard calibrated radioactive sources: ^{22}Na, ^{60}Co, ^{88}Y, ^{133}Ba, ^{137}Cs, ^{241}Am, ^{152}Eu, and ^{155}Eu. The measured efficiency curve at 20 cm is presented in Fig. 5.

The γ-ray spectrum for the neutron activated Ga sample ($^{nat}Ga_2O_3$ no. 2) is presented in Fig. 6, where the full-energy peaks of ^{70}Ga and ^{72}Ga are labeled. Figure 7 presents the decay curves of the 176.3- and 1039.5-keV γ lines of ^{70}Ga, showing an excellent agreement with the adopted ^{70}Ga half-life of 21.14(5) min. [17]. The numbers of activated ^{70}Ga nuclei derived from each of the two transitions, using the

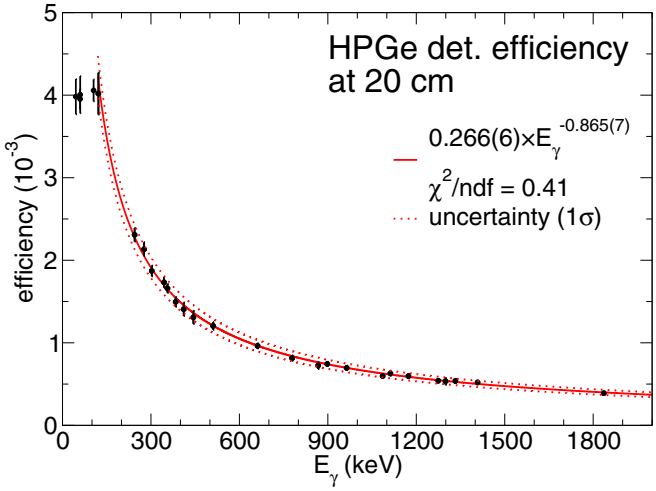

FIG. 5. Efficiency of the HPGe detector used at a distance of 20 cm (black dots with 1σ uncertainties) determined by standard calibrated radioactive sources: ^{22}Na, ^{60}Co, ^{88}Y, ^{133}Ba, ^{137}Cs, ^{241}Am, ^{152}Eu, and ^{155}Eu. The red curve is a fit to the data with the expression: $\epsilon = a \times E_\gamma^{-b}$ and the dotted lines are the uncertainty (1σ). The main source of the efficiency uncertainty is the radioactive source activity; these uncertainties are given by the source manufacturers. The small value of the reduced chi square suggests that these uncertainties are overestimated.

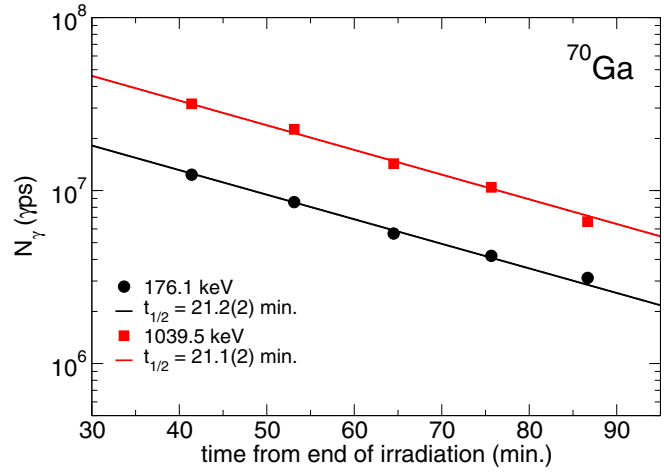

FIG. 7. Decay curves for ^{70}Ga. The uncertainties of each data point in this plot are only the statistical uncertainties of the activity measurement. $N_\gamma = N_{\rm act} I_\gamma$ [see Eq. (2)] is the photon intensity (γs per second) of the γ transitions at the 176.3- and 1039.5-keV lines of the ^{70}Ga decay, determined by γ spectrometry. Excellent agreement is observed with the adopted half-life of ^{70}Ga from the literature [21.14(5) min. [17]], and between the number of activated ^{70}Ga nuclei (see Tables III and IV) derived independently from each transition, using the respective adopted γ intensities [17]; see text.

adopted γ intensities [17], are in excellent agreement as well. The ratio of the 1039- and 176-keV γ ray intensities determined here, 2.53(6), is in agreement with and more precise than the ratio of the adopted intensities, 2.24(19) [17]. The reported γ intensity ratio in [18] is 2.30(6). The precise counting of activated ^{70}Ga nuclei, in spite of its short half-life relative to the irradiation time and the very low intensity of the γ transitions (Table II), is credited to the high intensity of the LiLiT neutron source. The SARAF-LiLiT setup was

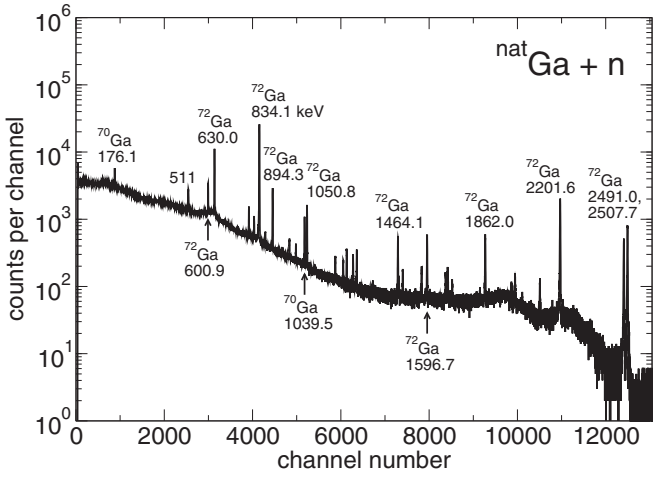

FIG. 6. γ-ray spectrum of the activated $^{\rm nat}Ga_2O_3$ no. 2 sample. The spectrum was accumulated for 3000 s, starting 2464 s after the end of the neutron activation. The sample was located 20 cm from the HPGe detector. The main Ga isotope full-energy peaks, with energies in keV, are labeled.

shown to produce high-energy γ rays, $\approx 10^8$ of 14.6 and 17.6 MeV γ rays/(mA $\times$ s), via the ^{7}Li$(p,\gamma)^8$Be reaction [9,19]. In cases where there are a stable A-1 isotope, an unstable A isotope, and a stable A+1 isotope, the nuclide A can be produced through the A $-$ 1(n,γ) or A + 1(γ,n) reactions. To test the possible contribution of the ^{71}Ga(γ,n) reaction to the production of ^{70}Ga, an irradiation of protons on LiLiT was conducted below the neutron production threshold. This resulted in the irradiation of the Ga sample ($^{\rm nat}Ga_2O_3$ no. 1) with γ rays, but without neutrons. The proton energy was measured to be 1800 keV. The total integrated current in this irradiation was $\approx$0.46 mA $\times$ h. The γ-ray spectrum for the activated Ga sample ($^{\rm nat}Ga_2O_3$ no. 1) is presented in Fig. 8. As can be seen, no Ga isotopes were created through (γ,n) reactions.

V. ACTIVATION RESULTS

The number of activated nuclei created during the irradiation, $N_{\rm act}$, was obtained from the γ-ray spectra using Eq. (2),

$$N_{\rm act} = \frac{C}{\epsilon_\gamma I_\gamma K_\gamma} \frac{e^{\lambda t_{\rm cool}}}{1 - e^{-\lambda t_{\rm real}}} \frac{t_{\rm real}}{t_{\rm live}} \frac{1}{f_b}, \qquad (2)$$

where C is the number of counts in a full-energy peak, ϵ_γ is the detector energy-dependent full-energy efficiency for the relevant target-detector geometry, and I_γ is the γ intensity per decay. The I_γ used in this work was taken from [17,20,21]. The correction due to γ-ray self-absorption in the sample is K_γ. In the case of a disk sample of thickness x, $K_\gamma \approx \frac{1-e^{-\mu x}}{\mu x}$, where μ is the γ-ray absorption coefficient. The γ-ray absorption coefficients μ were taken from [22]. The decay constant of the activated nucleus is $\lambda = \frac{\ln(2)}{t_{1/2}}$. The cooling time between

TABLE III. Analysis of one of the γ-ray spectra from the $^{nat}Ga_2O_3$ no. 2 sample, measured 5180 s after the end of the neutron irradiation, with 656.8 s real time and 600 s live time; see Eq. (2) for the definition of notations. The data for E_γ and I_γ were taken from [17,21].

Nucleus	E_γ (keV)	Counts	I_γ (%)	ϵ_γ (10^{-4})	K_γ	f_b	N_{act} (10^9)
^{70}Ga	176.115(13)	1264(93)	0.29(1)	30.4(8)	0.970(3)	0.550	16.4(14)
	1039.513(10)	602(43)	0.65(5)	6.50(8)	0.990(3)	0.550	16.1(17)
^{72}Ga	600.912(15)	3578(99)	5.822(19)	10.5(1)	0.987(3)	0.984	7.96(24)
	629.967(19)	15484(157)	26.13(4)	10.0(1)	0.987(3)	0.984	8.00(12)
	834.13(4)	45243(224)	95.45(8)	7.87(9)	0.989(3)	0.984	8.15(10)
	894.327(18)	4419(80)	10.136(15)	7.41(9)	0.989(3)	0.984	7.96(17)
	1050.794(17)	2643(64)	6.991(11)	6.44(8)	0.990(3)	0.984	7.93(22)
	1861.996(18)	1248(46)	5.41(3)	3.92(8)	0.992(3)	0.984	7.93(17)
	2201.586(17)	5479(79)	26.87(12)	3.39(7)	0.993(3)	0.984	8.10(21)
	2491.026(17)	1437(42)	7.73(3)	3.05(6)	0.993(3)	0.984	8.22(29)
	2507.718(17)	2454(52)	13.33(6)	3.03(6)	0.993(3)	0.984	8.19(25)

the end of the irradiation and the start of activity measurement is t_{cool}, and t_{real} (t_{live}) is the real (live) measurement time. The decay of activated nuclei during the irradiation is accounted for in f_b. It is calculated using the time dependence of the neutron yield $\Phi(t)$, obtained from the fission chamber (see Fig. 4), by $f_b = \frac{\int_0^{t_a} \Phi(t) e^{-\lambda(t_a - t)} dt}{\int_0^{t_a} \Phi(t) dt}$. t_a is the time of the end of irradiation. The decay parameters and correction factors used in this analysis are listed in Tables II and III. The numbers of activated nuclei at the end of the irradiation, N_{act}, calculated with Eq. (2), are summarized in Table IV.

VI. EXPERIMENTAL CROSS SECTION

Since the sample cross section is measured relative to the Au cross section (which is considered known), the cross section of the sample, averaged over the experimental neutron spectrum, can be expressed as

$$\sigma_{expt}(i) = \sigma_{ENDF}(\mathrm{Au}) \frac{N_{act}(i)}{N_{act}(\mathrm{Au})} \frac{n_t(\mathrm{Au})}{n_t(i)}, \quad (3)$$

where i denotes the Ga stable isotope (69 or 71) and $\sigma_{ENDF}(\mathrm{Au})$ is the reference Au cross section from the ENDF/B-VIII.0 library [23] averaged over the experimental neutron spectrum. It is defined as

$$\sigma_{ENDF}(\mathrm{Au}) = \frac{\int \sigma_{ENDF}(E_n; \mathrm{Au}) \frac{dn}{dE_n} dE_n}{\int \frac{dn}{dE_n} dE_n}. \quad (4)$$

The energy-dependent $^{197}\mathrm{Au}(n,\gamma)^{198}\mathrm{Au}$ cross section $\sigma_{ENDF}(E_n; \mathrm{Au})$ was taken from ENDF/B-VIII.0 [23], in agreement with high-precision experimental data [24,25].

TABLE IV. The number of activated nuclei at the end of the irradiation, N_{act}, and comparison with simulated N_{act}.

Sample	Nucleus	N_{act} (10^9)	Simulated N_{act} (10^9)
Au no. 14	^{198}Au	4.07(8)	4.09
$^{nat}Ga_2O_3$ no. 2	^{70}Ga	16.3(7)	
	^{72}Ga	8.1(1)	
Au no. 15	^{198}Au	3.65(6)	3.63

The neutron spectrum, $\frac{dn}{dE_n}$, is obtained from our simulation code (Fig. 9), developed and benchmarked by experiment [9,19,26,27]. The simulated neutron spectrum impinging on the Ga target, along with a $kT = 41.8$-keV fit to a Maxwellian neutron flux ($\propto E e^{-E/kT}$), is presented in Fig. 9. This spectrum is generated by a GEANT4 [28] simulation, using the SimLiT code [27] output as the neutron source. The SimLiT calculation uses $^7\mathrm{Li}(p,n)$ differential cross sections taken from [29] and takes into account the proton mean beam energy and energy spread, proton energy loss in the liquid Li using differential dE/dx values taken from SRIM [30], and a Gaussian proton beam profile consistent with the Au monitor autoradiography (Fig. 3). The detailed GEANT4 simulation takes into account the LiLiT geometry setup including the off-center position of the neutron beam relative to the Au-Ga-Au target and the surrounding materials. The simulation explicitly calculates (see [9,19] for details) the number of activated ^{198}Au nuclei, based on the $\sigma_{ENDF}(E_n; \mathrm{Au})$ cross sections and the measured proton charge during

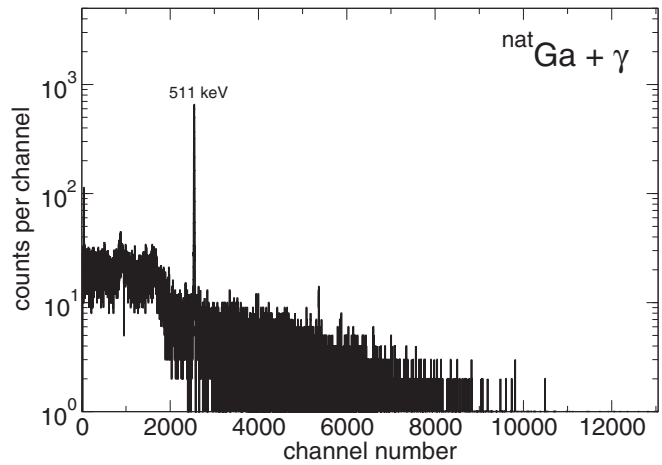

FIG. 8. Secondary γ-ray spectrum of the $^{nat}Ga_2O_3$ no. 1 sample after irradiation with primary γ rays. The spectrum was accumulated for 636 s, starting 1275 s after the end of the irradiation. The proton energy was below the neutron production threshold, resulting in the production of only γ rays. The sample was located 2 cm from the HPGe detector. No Ga lines are observed.

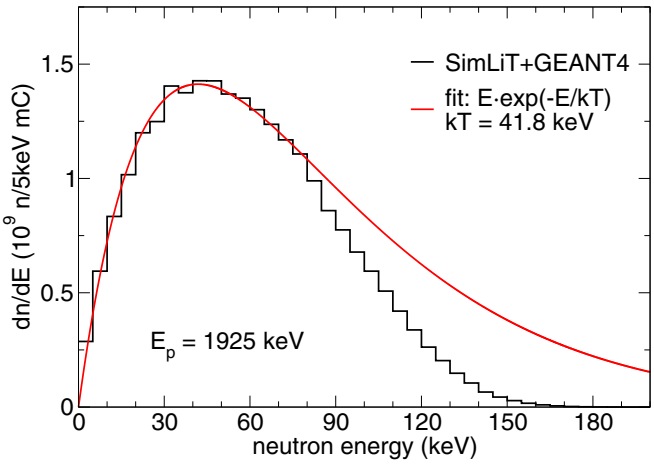

FIG. 9. The simulated neutron spectrum impinging on the Ga target (black). Also shown is a fit (between 0 and 90 keV) to a Maxwell-Boltzmann (MB) flux (red), where the best fit is for $kT = 41.8$ keV.

irradiation and reproduces the experimental ^{198}Au activity of the Au monitors within 0.5% (Table IV).

The results of the experimental cross sections, $\sigma_{\rm expt}$, of ^{69}Ga and ^{71}Ga [Eq. (3)] and of the $\sigma_{\rm ENDF}$(Au) values [Eq. (4)] are presented in Table V.

VII. MAXWELLIAN AVERAGED CROSS SECTION

The Maxwellian averaged cross section (MACS) at a given thermal energy kT is defined as

$$\langle\sigma\rangle_{kT} = \frac{\langle\sigma v\rangle}{v_T} = \frac{2}{\sqrt{\pi}}\frac{\int_0^\infty \sigma(E_n)E_n e^{-E_n/kT}dE_n}{\int_0^\infty E_n e^{-E_n/kT}dE_n}, \quad (5)$$

where $\sigma(E_n)$ is the differential (n,γ) reaction cross section at neutron energy E_n. In this work, the MACS at a given thermal energy kT is calculated with the procedure developed in [9,19,31] and using Eq. (6),

$$\mathrm{MACS}_{\rm expt}(kT) = \frac{2}{\sqrt{\pi}}C_{\rm lib}(kT)\sigma_{\rm expt}, \quad (6)$$

where the correction factor $C_{\rm lib}(kT)$ is given by Eq. (7):

$$C_{\rm lib}(kT) = \frac{\frac{\int_0^\infty \sigma_{\rm lib}(E_n)E_n e^{-E_n/kT}dE_n}{\int_0^\infty E_n e^{-E_n/kT}dE_n}}{\frac{\int_0^\infty \sigma_{\rm lib}(E_n)\frac{dn}{dE_n}dE_n}{\int_0^\infty \frac{dn}{dE_n}dE_n}}. \quad (7)$$

TABLE V. The experimental cross sections, $\sigma_{\rm expt}$ [Eq. (3)], measured in this work for the ^{69,71}Ga$(n,\gamma)^{70,72}$Ga reactions, together with the $\sigma_{\rm ENDF}$ cross section averaged over the neutron energy distribution (Fig. 9). See Table VII for explanation of $\sigma_{\rm ENDF}(^{197}$Au) uncertainty.

Isotope	$\sigma_{\rm expt}$ (mb)	$\sigma_{\rm ENDF}$ (mb)
^{197}Au		524(10)
^{69}Ga	119(5)	103
^{71}Ga	89(2)	107

TABLE VI. Comparison of correction factors, $C_{\rm lib}$, and MACS calculated for ^{69}Ga and ^{71}Ga at 30 keV using the different libraries [23,32–35]. See text for explanation.

	$C_{\rm lib}$		$\mathrm{MACS}_{\rm expt}$ (mb)	
Library	^{69}Ga	^{71}Ga	^{69}Ga	^{71}Ga
ENDF/B-VIII.0 [23]	1.03	1.02	138	103
JENDL-4.0 [32]	1.03	1.01	138	102
JEFF-3.3 [33]	1.0	0.97	134	98
CENDL-3.2 [34]	0.99	1.08	133	108
TENDL-2019 [35]	1.04	1.15	139	115
Average	1.018	1.046	136.4	105.0
Standard deviation	0.02	0.07	2.8	6.7

In Eq. (7), $\frac{dn}{dE_n}$ is the simulated experimental neutron spectrum (Fig. 9) and $\sigma_{\rm lib}(E_n)$ is the energy-dependent neutron capture cross section taken from an evaluation library.

In Table VI we present the correction factors, $C_{\rm lib}$, and the $\mathrm{MACS}_{\rm expt}$ at $kT = 30$ keV, calculated with Eq. (6), for the Ga isotopes. The $\mathrm{MACS}_{\rm expt}$ at $kT = 30$ keV derived in this work are obtained by using in Eq. (6) the average $C_{\rm lib}$ calculated using the various cross section libraries: ENDF/B-VIII.0 [23], JENDL-4.0 [32], JEFF-3.3 [33], CENDL-3.2 [34], and TENDL-2019 [35] (see Table VI).

The experimental uncertainties, as discussed in detail in [9,19], are summarized in Table VII. The uncertainties for the average $C_{\rm lib}$ were obtained by taking the standard deviation of the $C_{\rm lib}$ calculated for the various cross section libraries [23,32–35] (see Table VI).

TABLE VII. Random (rand) and systematic (sys) uncertainties in the results presented in this work.

	Uncertainty (%)			
	^{69}Ga		^{71}Ga	
Source of uncertainty	rand	sys	rand	sys
Target thickness	0.5		0.5	
Activity measurement	4.0		0.5	
Full-energy eff. rel. to Au		0.5[a]		0.5[a]
Intensity per decay		3.4		0.1
$\sigma_{\rm ENDF}$(Au)		1.9[b]		1.9[b]
$C_{\rm lib}$		2.0		6.4
Total random uncertainty	4.0		0.7	
Total systematic uncertainty		4.4		6.7
Total uncertainty	6.0		6.7	

[a]This contribution to the uncertainty of the ^{69,71}Ga MACS includes only the ratio of the full-energy efficiencies of the ^{69,71}Ga γ lines to that of the ^{198}Au γ line. In Tables III and IV the overall uncertainty (including the systematic uncertainty of the calibration sources) is quoted.

[b]This value includes the uncertainty of beam parameters (proton beam energy, energy spread, and distance of sample from Li) of 0.6%, the uncertainty of the simulations of 1.5% and the uncertainty of the ENDF cross section for Au of 1.0%, $\sqrt{0.6^2+1.5^2+1.0^2} = 1.9\%$. See [9] for more details of the uncertainties.

TABLE VIII. Comparison of the results of this work with previous experiments and compilations. The MACSs listed in the table correspond to $kT = 30$ keV. The previously measured MACSs were renormalized as specified in [36] using the recent measured ^{197}Au$(n,\gamma)^{198}$Au cross section data [24,25,37] used as standard. The KADoNiS v0.3 [5] recommended MACS (30 keV) is the average of the experimental data renormalized to the ^{197}Au$(n,\gamma)^{198}$Au MACS data measured in [38]. The KADoNiS v1.0 [36] recommended MACS (30 keV) values are an average from evaluated libraries ENDF/B-VII.1 [39], JENDL-4.0 [32], and TENDL-2015 [40].

	KADoNiS v0.3 [5]	KADoNiS v1.0 [36]	Walter, 1984 [4]	Anand *et al.*, 1979 [6]	Walter *et al.*, 1986 [7]	Göbel *et al.*, 2021 [8]	This work
MACS (^{69}Ga) (mb)	139(6)	123(9)	149(6)				136(8)
$\sigma_{exp}(^{69}\text{Ga})/\sigma_{exp}(^{197}\text{Au})$[a]						0.286(19)	0.227(12)
MACS (^{71}Ga) (mb)	123(8)	103(14)		79(23)	130(8)		105(7)
$\sigma_{exp}(^{71}\text{Ga})/\sigma_{exp}(^{197}\text{Au})$[a]						0.173(11)	0.170(5)

[a]Note that Göbel *et al.* [8] denote σ_{expt} as defined in Eq. (3) by SACS (spectrum averaged cross section) for their experimental neutron spectrum.

VIII. DISCUSSION

This work's results are compared in Table VIII and Fig. 10 with previously measured MACS at $kT = 30$ keV for ^{69}Ga [4] and ^{71}Ga [6,7], and with compilations of experimental values (KADoNiS v0.3 [5]) and of evaluated values (KADoNiS v1.0 [36]). We compare also the ratios $\sigma_{\text{expt}}(^{A}\text{Ga})/\sigma_{\text{expt}}(^{197}\text{Au})$ with the corresponding values from Göbel *et al.* [8], denoted there as SACS(^{A}Ga)/SACS(^{197}Au), calculated for the relevant experimental spectrum.

Our results for the ^{69}Ga MACS (30 keV) are in good agreement within uncertainties with the previous experimental value of [4] and those recommended by Bao *et al.* [41] and KADoNiS v0.3 [5]. Our MACS value for ^{71}Ga is larger than the experimental value of [6], but smaller than the experimental value of [7] recommended by Bao *et al.* [41] and KADoNiS v0.3 [5], though marginally consistent within the quoted uncertainties. This smaller value is significant in view of the fact that the previous value of KADoNiS v0.3 [5] was used in extensive network calculations [3]; see below. Both ^{69,71}Ga MACS values extracted in this work are in reasonable agreement with the evaluated values of KADoNiS v1.0 [36]. We note also the good agreement of our $\sigma_{\text{expt}}(^{71}\text{Ga})/\sigma_{\text{expt}}(^{197}\text{Au})$ value with that of Göbel *et al.* [8], but a striking discrepancy for $\sigma_{\text{expt}}(^{69}\text{Ga})/\sigma_{\text{expt}}(^{197}\text{Au})$, whose origin is not understood.

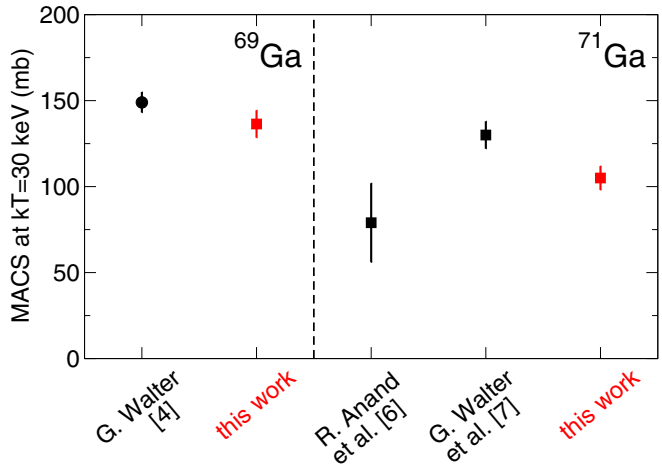

FIG. 10. Comparison of this work's results (red) with previously measured MACS at $kT = 30$ keV (black) for ^{69}Ga [4] (left) and ^{71}Ga [6,7] (right). The previously measured MACSs were renormalized as specified in the KADoNiS v1.0 website [36]. The TOF measurement is displayed as a circle and the activation measurements as squares.

Gallium, like the other elements between iron and strontium ($26 < Z < 38$, $60 \lesssim A \lesssim 90$), is produced primarily by the weak component of the *s* process in massive stars ($M_{\text{initial}} > 8M_{\odot}$) ([42] and references therein). Pignatari *et al.* [3] studied nucleosynthesis, including the weak *s* process, in a model of a population I (solar metallicity) $25M_{\odot}$ star. For the ^{69,71}Ga(n,γ) MACS, the authors used the values recommended by Bao *et al.* [41] (KADoNiS 0.3 [5]). As shown in Table VIII and discussed above, the new ^{69}Ga MACS measurement presented here supports the Bao *et al.* [41] value, but the ^{71}Ga MACS is 15% lower. This means that less ^{71}Ga is consumed by the (n,γ) reaction and hence its isotopic fraction is expected to increase compared to that calculated by Pignatari *et al.* [3]. In addition, since the *s* process flow goes from Ga to Ge, ^{69}Ga$(n,\gamma)^{70}$Ga$(\beta^-)^{70}$Ge, and ^{71}Ga$(n,\gamma)^{72}$Ga$(\beta^-)^{72}$Ge (see Fig. 1), the lower ^{71}Ga MACS is expected to result in a lower production of ^{72,73,74}Ge and reduce their isotopic fraction. The lower ^{71}Ga MACS (105(7) mb) may have as well a wider effect, as Pignatari *et al.* [3] concluded that the effects of MACS $\lesssim 150$ mb tend to propagate to heavier isotopes. However, we should caution that the above potential effects are tentative. The only way to check for the effect of the new ^{71}Ga MACS is to incorporate it in a network calculation like the one performed by Pignatari *et al.* [3].

Such nucleosynthesis models need to be tested against isotopic compositions in the relevant star types. This is done for many elements by isotopic analysis of chemical elements in presolar grains. However, to date, there are no measurements of Ga in presolar grains ([43–45]). The most studied family of presolar grains are the carbides, mainly SiC and graphite. At the same time, Ga is thought to usually not form carbides [46], so it is unlikely that there is enough Ga in presolar carbides for isotopic analysis with the current capabilities of the experimental techniques used. On the other hand, Lodders [47] calculated that Ga condensed in the early solar system as a trace element into the mineral feldspar, by substituting for the major element Al in the crystal lattice, and into Fe metal to a lesser extent. While presolar

feldspar has not been found to date, most of the presolar oxides and silicates studied to date contain Al as a major element. This makes them more likely hosts for stellar Ga to be analyzed.

IX. SUMMARY

The neutron capture cross sections of ^{69,71}Ga were measured by the activation technique in the intense $kT \approx$ 40-keV quasi-Maxwellian neutron field of the SARAF-LiLiT facility. The reaction products were measured by γ spectrometry with a HPGe detector. The experimental cross sections were converted to Maxwell-averaged cross sections at $kT = 30$ keV using the energy dependence of various neutron cross section library data. The MACS values obtained in this work are MACS (^{69}Ga) = 136(8) mb and MACS (^{71}Ga) = 105(7) mb. The ^{69}Ga MACS value is in good agreement with previous experimental values and their recommended values while that of ^{71}Ga is smaller and with reduced uncertainty than the experimental recommended value. This smaller value may have implications in network calculations such as those of Pignatari *et al.* [3] which used so far the recommended values. Potential natural samples to measure stellar Ga composition are presolar silicates and oxides, in which Ga may replace Al in the grains' crystal lattice. We note a significant and not understood discrepancy between our experimental cross-section value of ^{69}Ga with that recently published by Göbel *et al.* [8], beyond that expected from the different experimental conditions.

ACKNOWLEDGMENTS

We would like to thank the SARAF and LiLiT (Soreq NRC) staffs for their dedicated help during the experiments. This work was supported in part by Israel Science Foundation (Grant No. 1387/15) and the Pazy Foundation (Israel). M.P. acknowledges support by the European Union (ChETEC-INFRA, Project No. 101008324).

[1] F. Käppeler, R. Gallino, S. Bisterzo, and W. Aoki, Rev. Mod. Phys. **83**, 157 (2011).
[2] R. Reifarth, C. Lederer, and F. Käppeler, J. Phys. G **41**, 053101 (2014).
[3] M. Pignatari, R. Gallino, M. Heil, M. Wiescher, F. Käppeler, F. Herwig, and S. Bisterzo, Astrophys. J. **710**, 1557 (2010).
[4] G. Walter, Tech. Rep. No. KfK-3706, Forschungszentrum Karlsruhe, 1984.
[5] I. Dillmann, R. Plag, F. Käppeler, and T. Rauscher, in *EFNUDAT Fast Neutrons - Scientific Workshop on Neutron Measurements, Theory & Applications* (JRC-IRMM, Geel, Belgium, 2009), available online: http://www.kadonis.org/.
[6] R. P. Anand, M. L. Jhingan, D. Bhattacharya, and E. Kondaiah, Nuovo Cimento A **50**, 247 (1979).
[7] G. Walter, H. Beer, F. Käppeler, G. Reffo, and F. Fabbri, Astron. Astrophys. **167**, 186 (1986).
[8] K. Göbel, C. Beinrucker, B. Brückner, P. Erbacher, S. Fiebiger, M. Fonseca, M. Heftrich, T. Heftrich, F. Käppeler, A. Krása, D. Kurtulgil, C. Lederer-Woods, R. Plag, A. Plompen, R. Reifarth, S. Schmidt, K. Sonnabend, and M. Weigand, Phys. Rev. C **103**, 025802 (2021).
[9] M. Paul, M. Tessler, M. Friedman, S. Halfon, T. Palchan, L. Weissman, A. Arenshtam, D. Berkovits, Y. Eisen, I. Eliahu, G. Feinberg, D. Kijel, A. Kreisel, I. Mardor, G. Shimel, A. Shor, and I. Silverman, Eur. Phys. J. A **55**, 44 (2019).
[10] S. Halfon, A. Arenshtam, D. Kijel, M. Paul, D. Berkovits, I. Eliyahu, G. Feinberg, M. Friedman, N. Hazenshprung, I. Mardor, A. Nagler, G. Shimel, M. Tessler, and I. Silverman, Rev. Sci. Instrum. **84**, 123507 (2013).
[11] S. Halfon, A. Arenshtam, D. Kijel, M. Paul, L. Weissman, O. Aviv, D. Berkovits, O. Dudovitch, Y. Eisen, I. Eliyahu, G. Feinberg, G. Haquin, N. Hazenshprung, A. Kreisel, I. Mardor, G. Shimel, A. Shor, I. Silverman, M. Tessler, and Z. Yungrais, Rev. Sci. Instrum. **85**, 056105 (2014).
[12] A. Kreisel, L. Weissman, A. Arenshtam, Y. B. Aliz, D. Berkovits, Y. Buzaglo, O. Dudovich, Y. Eisen, I. Eliyahu, G. Feinberg, I. Fishman, I. Gertz, A. Grin, S. Halfon, Y. Haruvy, T. Hirsh, D. Hirschmann, Z. Horvitz, B. Kaizer, D. Kijel *et al.*, in *Proceedings of LINAC 2014*, edited by C. Carli, M. Draper, Y.-M. Ducimetiere, A. McCausey, R. Müller, J. Poole, V. R. W. Schaa (Geneva, Switzerland, 2014), pp. 770–774.
[13] I. Mardor, D. Berkovits, S. Halfon, T. Hirsh, Y. Mishnayot, I. Silverman, S. Vaintraub, L. Weissman, M. Hass, I. Mukul, B. Ohayon, M. Paul, G. Ron, M. Tessler, and T. Dickel, in *Proceedings of the 26th International Nuclear Physics Conference*, edited by A. Thomas *et al.*, Contribution 109 (SISSA, Adelaide, Australia, 2016).
[14] I. Mardor, O. Aviv, M. Avrigeanu, D. Berkovits, A. Dahan, T. Dickel, I. Eliyahu, M. Gai, I. Gavish-Segev, S. Halfon, M. Hass, T. Hirsh, B. Kaiser, D. Kijel, A. Kreisel, Y. Mishnayot, I. Mukul, B. Ohayon, M. Paul, A. Perry *et al.*, Eur. Phys. J. A **54**, 91 (2018).
[15] Sigma-Aldrich Co., https://www.sigmaaldrich.com/catalog/product/aldrich/215066.
[16] G. Feinberg, Study of the 7Li(p,n) Reaction Towards Measurements of Neutron-Capture Cross Sections in the Astrophysical s-process With the SARAF Accelerator and a Liquid-Lithium Target, Ph.D. thesis, The Hebrew University of Jerusalem, 2014, available online: http://arad.mscc.huji.ac.il/dissertations/W/JSL/001975970.pdf.
[17] G. Gürdal and E. McCutchan, Nucl. Data Sheets **136**, 1 (2016).
[18] U. J. Schrewe and W. D. Schmidt-Ott, Z. Phys. A **281**, 125 (1977).
[19] M. Tessler, M. Paul, A. Arenshtam, G. Feinberg, M. Friedman, S. Halfon, D. Kijel, L. Weissman, O. Aviv, D. Berkovits, Y. Eisen, I. Eliyahu, G. Haquin, A. Kreisel, I. Mardor, G. Shimel, A. Shor, I. Silverman, and Z. Yungrais, Phys. Lett. B **751**, 418 (2015).

[20] H. Xiaolong, Nucl. Data Sheets **110**, 2533 (2009).
[21] D. Abriola and A. Sonzogni, Nucl. Data Sheets **111**, 1 (2010).
[22] J. Hubbell and S. Seltzer, Tables of X-Ray Mass Attenuation Coefficients and Mass Energy-Absorption Coefficients, NIST Standard Reference Database 126 (version 1.4) (National Institute of Standards and Technology, Gaithersburg, MD, 2004), technical report, DOI:https://dx.doi.org/10.18434/T4D01F.
[23] D. Brown, M. Chadwick, R. Capote, A. Kahler, A. Trkov, M. Herman, A. Sonzogni, Y. Danon, A. Carlson, M. Dunn, D. Smith, G. Hale, G. Arbanas, R. Arcilla, C. Bates, B. Beck, B. Becker, F. Brown, R. Casperson, J. Conlin *et al.*, Nucl. Data Sheets **148**, 1 (2018).
[24] C. Lederer, N. Colonna, C. Domingo-Pardo, F. Gunsing, F. Käppeler, C. Massimi, A. Mengoni, A. Wallner, U. Abbondanno, G. Aerts, H. Álvarez, F. Álvarez-Velarde, S. Andriamonje, J. Andrzejewski, P. Assimakopoulos, L. Audouin, G. Badurek, M. Barbagallo, P. Baumann, F. Becvar *et al.* (n_TOF Collaboration), Phys. Rev. C **83**, 034608 (2011).
[25] C. Massimi, B. Becker, E. Dupont, S. Kopecky, C. Lampoudis, R. Massarczyk, M. Moxon, V. Pronyaev, P. Schillebeeckx, I. Sirakov, and R. Wynants, Eur. Phys. J. A **50**, 124 (2014).
[26] G. Feinberg, M. Friedman, A. Krása, A. Shor, Y. Eisen, D. Berkovits, D. Cohen, G. Giorginis, T. Hirsh, M. Paul, A. J. M. Plompen, and E. Tsuk, Phys. Rev. C **85**, 055810 (2012).
[27] M. Friedman, D. Cohen, M. Paul, D. Berkovits, Y. Eisen, G. Feinberg, G. Giorginis, S. Halfon, A. Krása, A. Plompen, and A. Shor, Nucl. Instrum. Methods Phys. Res., Sect. A **698**, 117 (2013).
[28] S. Agostinelli, J. Allison, K. Amako, J. Apostolakis, H. Araujo, P. Arce, M. Asai, D. Axen, S. Banerjee, G. Barrand, F. Behner, L. Bellagamba, J. Boudreau, L. Broglia, A. Brunengo, H. Burkhardt, S. Chauvie, J. Chuma, R. Chytracek, G. Cooperman *et al.*, Nucl. Instrum. Methods Phys. Res., Sect. A **506**, 250 (2003).
[29] H. Liskien and A. Paulsen, At. Data Nucl. Data Tables **15**, 57 (1975).
[30] J. Ziegler, M. Ziegler, and J. Biersack, Nucl. Instrum. Methods Phys. Res., Sect. B **268**, 1818 (2010), 19th International Conference on Ion Beam Analysis.
[31] M. Tessler, M. Paul, S. Halfon, B. S. Meyer, R. Pardo, R. Purtschert, K. E. Rehm, R. Scott, M. Weigand, L. Weissman, S. Almaraz-Calderon, M. L. Avila, D. Baggenstos, P. Collon, N. Hazenshprung, Y. Kashiv, D. Kijel, A. Kreisel, R. Reifarth, D. Santiago-Gonzalez *et al.*, Phys. Rev. Lett. **121**, 112701 (2018).
[32] K. Shibata, O. Iwamoto, T. Nakagawa, N. Iwamoto, A. Ichihara, S. Kunieda, S. Chiba, K. Furutaka, N. Otuka, T. Ohasawa, T. Murata, H. Matsunobu, A. Zukeran, S. Kamada, and J. Katakura, J. Nucl. Sci. Technol. **48**, 1 (2011).
[33] A. J. M. Plompen, O. Cabellos, C. De Saint Jean, M. Fleming, A. Algora, M. Angelone, P. Archier, E. Bauge, O. Bersillon, A. Blokhin, F. Cantargi, A. Chebboubi, C. Diez, H. Duarte, E. Dupont, J. Dyrda, B. Erasmus, L. Fiorito, U. Fischer, D. Flammini *et al.*, Eur. Phys. J. A **56**, 181 (2020), data available online at: https://www.oecd-nea.org/dbdata/jeff/jeff33/index.html.
[34] Z. Ge, R. Xu, H. Wu, Y. Zhang, G. Chen, Y. Jin, N. Shu, Y. Chen, X. Tao, Y. Tian, P. Liu, J. Qian, J. Wang, H. Zhang, L. Liu, and X. Huang, EPJ Web Conf. **239**, 09001 (2020).
[35] A. Koning, D. Rochman, J.-Ch. Sublet, N. Dzysiuk, M. Fleming, and S. der Marck, Nucl. Data Sheets **155**, 1 (2019).
[36] Kadonis v1.0, available online: https://exp-astro.de/kadonis1.0/.
[37] C. Massimi, C. Domingo-Pardo, G. Vannini, L. Audouin, C. Guerrero, U. Abbondanno, G. Aerts, H. Álvarez, F. Álvarez-Velarde, S. Andriamonje, J. Andrzejewski, P. Assimakopoulos, G. Badurek, P. Baumann, F. Becvar, F. Belloni, E. Berthoumieux, F. Calviño, M. Calviani, D. Cano-Ott, and K. Wisshak (n_TOF Collaboration), Phys. Rev. C **81**, 044616 (2010).
[38] W. Ratynski and F. Käppeler, Phys. Rev. C **37**, 595 (1988).
[39] M. B. Chadwick, M. Herman, P. Obložinský, M. Dunn, Y. Danon, A. Kahler, D. Smith, B. Pritychenko, G. Arbanas, R. Arcilla, R. Brewer, D. Brown, R. Capote, A. Carlson, Y. Cho, H. Derrien, K. Guber, G. Hale, S. Hoblit, S. Holloway *et al.*, Nucl. Data Sheets **112**, 2887 (2011), special Issue on ENDF/B-VII.1 Library.
[40] A. Koning, D. Rochman, J. Kopecky, J. Sublet, M. Fleming, E. Bauge, S. Hilaire, P. Romain, B. Morillon, H. Duarte, S. van der Marck, S. Pomp, H. Sjostrand, R. Forrest, H. Henriksson, O. Cabellos, J. L. S. Goriely, A. P. H. Leeb, and R. Mills, Tendl-2015: Talys-based evaluated nuclear data library (2015).
[41] Z. Bao, H. Beer, F. Käppeler, F. Voss, K. Wisshak, and T. Rauscher, At. Data Nucl. Data Tables **76**, 70 (2000).
[42] F. Kappeler, H. Beer, and K. Wisshak, Rep. Prog. Phys. **52**, 945 (1989).
[43] K. M. Hynes and F. Gyngard, in *40th Lunar and Planetary Science Conference* (Lunar and Planetary Institute, Houston, 2009), Abstract No. 1198.
[44] T. Stephan, M. Bose, A. Boujibar, A. M. Davis, C. J. Dory, F. Gyngard, P. Hoppe, K. M. Hynes, N. Liu, L. R. Nittler, R. C. Ogliore, and R. Trappitsch, in *51st Lunar and Planetary Science Conference* (Lunar and Planetary Institute, Houston, 2020), Abstract No. 2140.
[45] Presolar grains database, https://presolar.physics.wustl.edu/presolar-grain-database/.
[46] V. B. Kumar, M. Monte, O. Mathon, S. Pascarelli, Z. Porat, and A. Gedanken, J. Am. Ceram. Soc. **100**, 3305 (2017).
[47] K. Lodders, Astrophys. J. **591**, 1220 (2003).